Check for updates



ADVANCED MATERIALS
www.advmat.de

# Bollard-Anchored Binder System for High-Loading Cathodes Fabricated via Dry Electrode Process for Li-Ion Batteries

*Jihyeon Kang, Hojong Eom, Seohyeon Jang, Doehyeob Yoo, Hyeonha Lee, Minju Kim, Myeong-Lok Seol, Jeong Woo Han,* Inho Nam,* and Hannah Song**

**The dry battery electrode (DBE) process offers significant advantages over conventional wet-coating methods for electrode fabrication. Unlike traditional processes that rely on toxic solvents such as N-methyl-2-pyrrolidone (NMP), the DBE technique uses solvent-free methods, reducing environmental impact and production costs while enhancing compatibility and performance. However, polytetrafluoroethylene (PTFE), the only binder currently used for large-scale DBE fabrication (binder fibrillation), faces potential regulatory restrictions under Polyfluoroalkyl Substances (PFAS) guidelines and limits Li-ion conductivity, elastomeric properties, and particle adhesion. This study explores a novel dual-binder system, termed the "bollard hitch" model, designed to overcome these limitations as the first PTFE-less binder for binder fibrillation. Poly(acrylic acid)-grafted sodium carboxymethyl cellulose (PC) acts as the "bollard," strongly attaching to the PTFE "anchor." This binder system reduces PTFE usage by over 70% and enables the fabrication of high-mass loading cathodes (up to 90 mg cm$^{-2}$, 15.6 mAh cm$^{-2}$) with superior performance. It enhances ionic conductivity and mechanical strength, making it suitable for high-voltage applications and offering great potential to revolutionize the manufacturing of high-performance, durable energy storage systems.**

## 1. Introduction

The design of next-generation batteries with enhanced safety, cost reduction, and eco-friendly manufacturing processes represents a new frontier in societal development and economic growth. Recently, the dry battery electrode (DBE) technique, originally developed for supercapacitor manufacturing,[1–4] has emerged as a promising method in the battery industry due to its distinct advantages over conventional wet-coating methods. This technique utilizes solvent-free processes that are environmentally friendly, reduce costs, improve compatibility and production efficiency, and enhance electrode performance.[5]

The DBE technique innovates electrode manufacturing routes, especially for cathode manufacturing, by shifting from the conventional "powder-slurry-film" method to a more concise "powder-film" method.[6] The conventional cathode "powder-slurry-film" processes have included the use of N-methyl-2-pyrrolidone (NMP) as a solvent for slurry production.[7,8] However, the high cost and toxicity of NMP require solvent recovery facilities for the collection of the evaporated NMP during the drying of the electrode. Consequently, the EU imposed regulations on the use of NMP in May 2020;[9] therefore, innovative steps are now required in the wet-coating processes for cathode production.

The DBE method offers fundamental benefits by simplifying manufacturing processes and reducing production costs (Figure S1, Supporting Information).[6,10,11] It also enables the production of high-mass loading electrodes—traditionally limited to under 20 mg cm$^{-2}$ in the "powder-slurry-film" method—thereby enhancing overall battery module performance.[12,13] In this context, the DBE technique also offers significant advantages in the aerospace

J. Kang, H. Eom, S. Jang, D. Yoo, I. Nam
Department of Chemical Engineering
Department of Advanced Materials Engineering
Department of Intelligent Energy and Industry
Chung-Ang University
Seoul 06974, Republic of Korea
E-mail: inhonam@cau.ac.kr

The ORCID identification number(s) for the author(s) of this article can be found under https://doi.org/10.1002/adma.202416872

© 2025 The Author(s). Advanced Materials published by Wiley-VCH GmbH. This is an open access article under the terms of the Creative Commons Attribution-NonCommercial License, which permits use, distribution and reproduction in any medium, provided the original work is properly cited and is not used for commercial purposes.

DOI: 10.1002/adma.202416872

H. Lee, M. Kim, H. Song
Battery Manufacturing Engineering R&D Team
Hyundai Motor Company
Uiwang, Gyeonggi 16082, Republic of Korea
E-mail: hannah.song@hyundai.com

M.-L. Seol
NASA Ames Research Center/USRA
Moffett Field, California 94035, USA

J. W. Han
Department of Materials Science and Engineering
Seoul National University
Seoul 08826, Republic of Korea
E-mail: jwhan98@snu.ac.kr

sector.[14–17] NASA's upcoming Artemis program aims to establish a base camp to support extended expeditions on the Moon's surface as part of broader space exploration efforts. A key aspect of the program is the simplification of battery manufacturing, achieved by reducing dependence on Earth-based supplies and utilizing in situ resource utilization (ISRU) materials.[18] The DBE technique facilitates this by minimizing the need for solvents and heating processes, which cannot be sourced from the Moon's surface.

DBE approach uses specialized fabrication methods, including powder compression, vapor deposition, powder spraying, and binder fibrillation. Among them, however, binder fibrillation is the only method that can fabricate large-area electrode sheets with precise control and at relatively low costs (see Note S1, Supporting Information).[19–25] To date, polytetrafluoroethylene (PTFE) has been also considered the only binder that can be used in the binder fibrillation method during DBE manufacturing.[26,27] PTFE exhibits relatively weak van der Waals attraction between its molecular chains because the high electronegativity of F draws electrons toward the C—F bond and weakens transient shifts in electron density.[28–30] This weak intermolecular attraction allows the polymer chains to readily unravel from PTFE particles like a "skein", forming what are referred to as "fibrils". Under shear force, the fibrils can connect electrode particles and spontaneously form electrode textiles or sheets.

Our previous study used binder fibrillation with PTFE and supplemented modified single-walled carbon nanotubes (CNTs) as conductive agents in the NMC as the cathode. This fabricated Li-ion batteries with a superior performance to those previously produced using DBE processes.[31] Ryu et al. also used CNT conductive materials to improve the electrical conductivity and mechanical strength of the cathode based on binder fibrillation.[32] However, these approaches are still impractical due to the high cost of conductive agents and the complexity of the modification processes, such as controlled ozone treatments.[33–36] These previous studies are very important, but there is a concern that it might overshadow other, potentially more critical, problems of PTFE itself.

The fibrillated PTFE binder used in the DBE method has several limitations, making it rarely practical for certain applications. Most notably, PTFE is likely to face regulation as a perfluoroalkyl substance (PFAS), similar to NMP, under strict environmental policies. The U.S. government has already designated some PFAS as hazardous under the Comprehensive Environmental Response, Compensation, and Liability Act (CERCLA).[37,38] Additionally, some EU nations are developing regulations that will ban the use of all PFAS, which includes fluoropolymers such as PTFE.[39] In response, many industries have already begun reducing their PTFE usage in anticipation of these restrictions. However, to the best of our knowledge, the development of PTFE-free or PTFE-less binders has not been widely recognized as a critical issue in the binder fibrillation process.

Using PTFE as a cathode binder also has technical drawbacks: 1) PTFE is prone to particle agglomeration, leading to inhomogeneous distribution of the active material, conductive agents, and binder; 2) its fully fluorinated main chain, combined with the absence of intermolecular hydrogen bonds, reduces ionic conductivity and particle adhesion;[40–42] 3) the low electron density of C—F bonds increase their susceptibility to interfacial degradation as they cannot effectively capture various active intermediates; and 4) its reactivity with the electrolyte leads to the formation of a thick solid-electrolyte interphase (SEI) layer.[43–48] Recent studies have also focused on enhancing anode stability using the binder fibrillation DBE method.[49,50] PTFE's low lowest unoccupied molecular orbital (LUMO) allows it to easily accept electrons, making stability issues when used in anodes.[51,52] Given these limitations and increasing regulatory pressures on substances like NMP and PFAS, the development of new PTFE-less or PTFE-free binders is urgently needed.[53,54]

In this study, we explore an optimal dual-binder system for cathode fibrillation to offset the drawbacks of the PTFE binder. To overcome the industrial costs and regulatory constraints, our focus shifted toward developing a DBE-specific PTFE-less binder that plays a significant role in dispersion control and compatibility with conventional conductive agents. Efficient binder additives were selected using the following criteria:[40] 1) high ionic conductivity; 2) strong adhesion between the electrode and current collector; and 3) electrochemical stability at high voltages. While the criteria are prevalent in Li-ion batteries that utilize conventional wet-coating methods, their application in the DBE process is relatively unexplored.

Our approach involves developing "micro bollards" to anchor PTFE fibrils, significantly reducing PTFE usage in NMC cathodes. Unlike the sheet-like connections formed by polyvinylidene fluoride (PVdF) binders in wet processes (**Figure 1**a,d), PTFE in dry processes forms bridge-like connections within the electrode (Figure 1b,e,g). The bollards, composed of poly(acrylic acid)-grafted sodium carboxymethyl cellulose (PAA-grafted CMC, also referred as PC), tightly adsorb onto the NMC surface through physicochemical interactions and anchor PTFE fibrils, enhancing the bonding between cathode materials (Figure 1c,f,h). The term "dual-binder", in this study, refer to the distinct interactions between PTFE and PC binders within the electrode. The PAA and CMC used in PC condensation reaction contain abundant polar functional groups, such as –OH and —COOH, which enhance ionic conductivity by facilitating the transfer of $Li^+$ ions between adjacent polar sites.[55–57] The PC forms strong chemical interactions with the oxide layer of NMC and the F atoms of PTFE, thereby improving adhesion between the active materials. This suppresses the detachment of PTFE and increases the durability of intermolecular interactions. As a result, the use of PTFE is minimized by its stronger connection to the bollard compared to its direct attachment to the NMC surface. This binder system, referred to as the "bollard hitch" model, is also investigated using deep-learning-based molecular dynamics (MD) simulations.

By using the PC structure as a "micro bollard," we demonstrated that stable electrode sheets can be formed via fibrillation, even with more than a 70% reduction in PTFE content (0.6 wt.% in the electrode). With an optimal PC:PTFE ratio of 7:3 (PC_PTFE73), we achieved a high mass loading of 30 mg $cm^{-2}$ for the NMC 622 cathode, delivering a superior capacity of 4.0 mAh $cm^{-2}$ at a high C-rate (2 C). This performance surpassed that of a PTFE-only cathode which required three times more PTFE binder (2 wt.% in the electrode). Additionally, an ultra-high loading cathode (90 mg $cm^{-2}$, 15.6 mAh $cm^{-2}$) was produced, outperforming previous studies (Tables S1 and S2, Supporting Information).[58–70] A full cell was successfully fabricated


© 2025 The Author(s). Advanced Materials published by Wiley-VCH GmbH

15214095, 2025, 12, Downloaded from https://advanced.onlinelibrary.wiley.com/doi/10.1002/adma.202416872 by Chung-Ang University, Seoul, Wiley Online Library on [23/10/2025]. See the Terms and Conditions (https://onlinelibrary.wiley.com/terms-and-conditions) on Wiley Online Library for rules of use; OA articles are governed by the applicable Creative Commons License

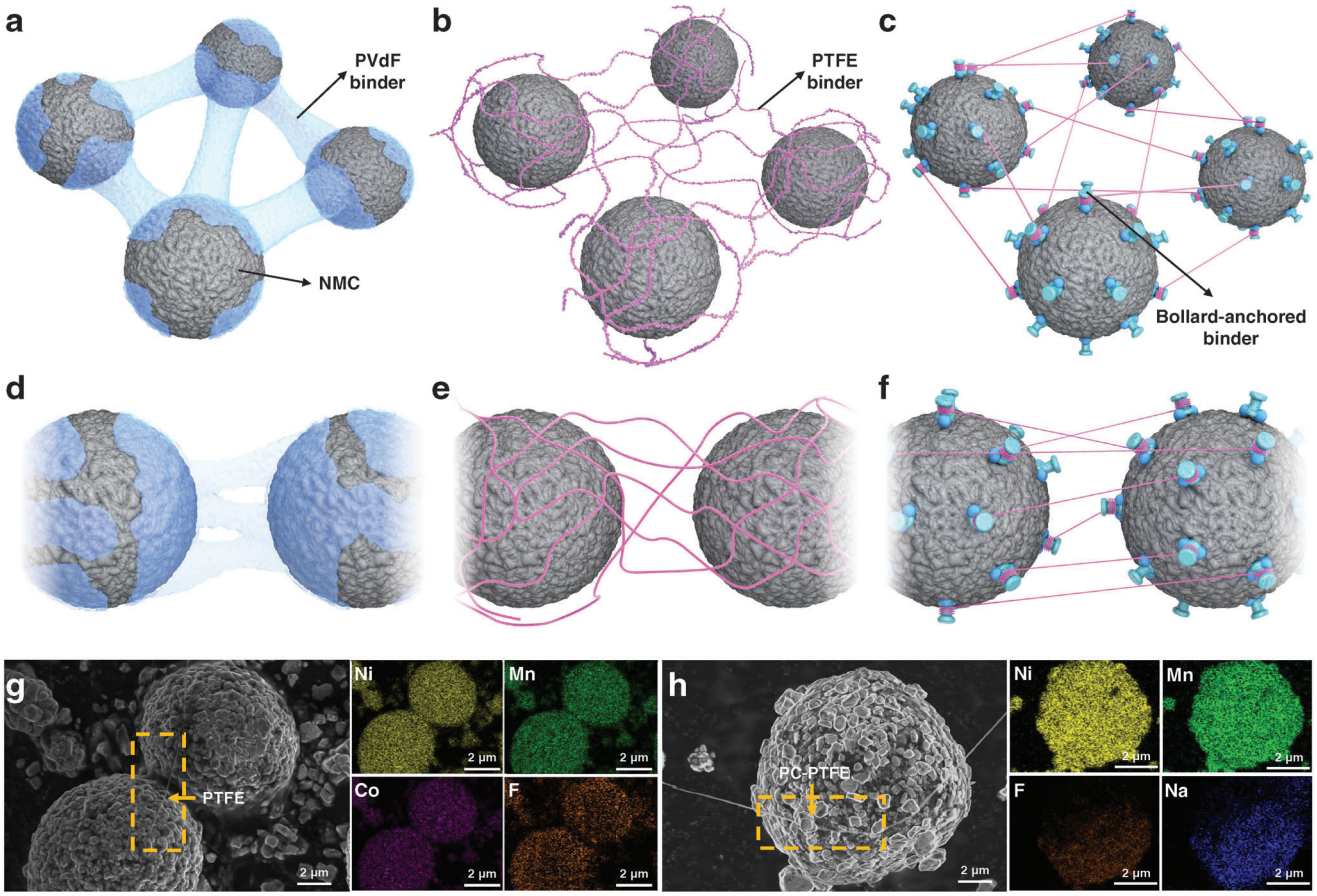



**Figure 1.** Schematic images of each binder in the cathode electrode: a) PVdF binder from the wet process, b) PTFE binder from the dry process, and c) PC_PTFE binder from the dry process. The binding mechanisms of each binder to electrode materials: d) PVdF binder, e) PTFE binder, and f) PC_PTFE binder. The actual behavior of binders as observed through FE-SEM: g) PTFE binder, and h) PC_PTFE binder in cathode mixture; The PTFE and PC_PTFE binders are indicated with arrows within the yellow dashed boxes.

using a solvent-free process for both the cathode and anode. The PC_PTFE73-equipped full cell showed a high-capacity retention of 84% after 50 cycles at 0.5 C, attributed to its enhanced ionic conductivity and stability at high voltage. Furthermore, the full cell with a slurry-cast graphite anode exhibited an 86% capacity retention over 100 cycles, an improvement over the PTFE-only cathode full cell. These findings can significantly impact the development of high-performance, durable energy storage systems, potentially revolutionizing the battery manufacturing industry.

## 2. Results and Discussion

### 2.1. Optimization of the Dry Electrode Process Based on the PTFE Binder

The operating mechanisms of two binders—PVdF and PTFE—are shown in Figure 1a,b,d,e. The first binder, PVdF, was used to create a sheet-like connection between the components in the electrode via the conventional wet-processing method. However, this connection restricted the $Li^+$ ion and electron transport, thereby reducing the efficiency of the kinetics of the electrode. This is not a major concern when the electrode is thin; however, its effect on the performance of a thick electrode is significant. The second binder, PTFE, was used to generate a bridge-like connection between the electrode constituents via the dry method (Figure 1b,e,g). The bridge-like connection provided by the fibrillated binder is a more desirable structure for facilitating the movement of the $Li^+$ ions and electrons in the cathode. The benefits of the bridge-like connections were observed in the specific-capacity data. PTFE exhibited a higher capacity than that of PVdF at all C-rates, with electrodes in the range of 15–30 mg $cm^{-2}$ (**Figure 2**a–i).

In the dry mixing process, increasing electrode loading without a solvent can result in the aggregation of cathode particles owing to electrostatic and van der Waals interactions, particularly when mixing is vigorous or prolonged. Also, precise control of mixing time and shear force is critical to prevent excessive fibrillation of PTFE, which may adversely affect the electrode's mechanical properties. The resulting mixture is inhomogeneous and exhibits a high standard deviation (STD) in cell capacity at high C-rates. The capacity of a 30 mg $cm^{-2}$ loading electrode was 103.65 mAh $g^{-1}$ (3.1 mAh $cm^{-2}$) ± 16.52 mAh $g^{-1}$ (± STD) at 2 C (Figure S2, Supporting Information). This STD was higher than that of the PVdF electrode (88.12 mAh $g^{-1}$, 2.6 mAh $cm^{-2}$; STD = 11.37 mAh $g^{-1}$; Figure 2g). Therefore, two common mixing methods[71]—planetary mixing and ball milling—were assessed


© 2025 The Author(s). Advanced Materials published by Wiley-VCH GmbH

15214095, 2025, 12, Downloaded from https://advanced.onlinelibrary.wiley.com/doi/10.1002/adma.202416872 by Chung-Ang University, Seoul, Wiley Online Library on [23/10/2025]. See the Terms and Conditions (https://onlinelibrary.wiley.com/terms-and-conditions) on Wiley Online Library for rules of use; OA articles are governed by the applicable Creative Commons License

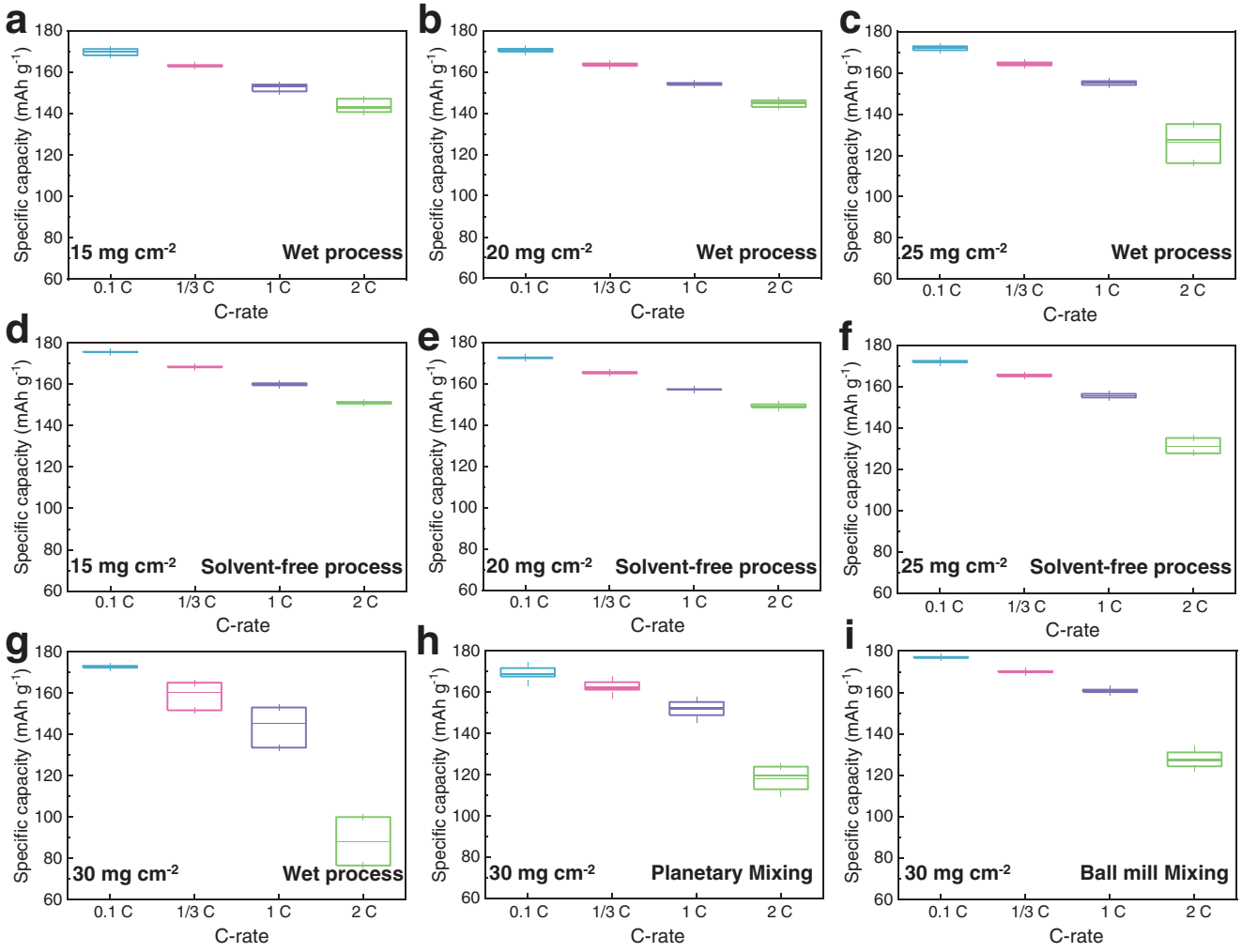



**Figure 2.** The capacity deviation was measured at varying C-rates (0.1 C, 1/3 C, 1 C, and 2 C) for a-c) the PVdF-based wet process and d–f) the PTFE-based solvent-free process loading amount from 15 to 30 mg $cm^{-2}$ (mixing was performed three times using a ball mill mixer). Capacity deviation at a 30 mg $cm^{-2}$ under different mixing processes for g) PVdF-based wet process, h) the PTFE-based solvent-free process with one-time mixing using a planetary mixer, and i) the PTFE-based solvent-free process with three-time mixing using a ball mill mixer.

to identify a suitable method for reducing the performance degradation caused by uneven dispersion during the dry process of cathode fabrication (for more details, see Note S2, Supporting Information). The planetary mixing method resulted in a capacity of 118.22 mAh $g^{-1}$ ± 5.59 mAh $g^{-1}$ (Figure 2h), whereas a capacity of 127.67 mAh $g^{-1}$ ± 4.28 mAh $g^{-1}$ was observed when the ball mill method was applied (Figure 2i). Both mixers exhibited improved performances and lower STDs than half of the values attained using PVdF. Consequently, mixing in triplicate using a ball mill was selected and used in subsequent experiments.

### 2.2. Identifying the Binder Additive for Improved Performance of Dry Battery Electrodes

The mechanical properties of the binder additive were examined and compared with those of a PTFE binder (selected as the control sample), thereby investigating its potential use as a cathode binder additive. PTFE consists solely of F atoms bonded to the carbon main chain.[40–42] This structure lacks the ability to form intermolecular hydrogen bonds, which results in reduced ionic conductivity and particle adhesion. Therefore, the additional binder should be compatible with the existing components, which also exhibit high ionic and electrical conductivity, mechanical stability, and strong adhesive properties. To meet these requirements, introducing binder additives with polar functional groups, such as —OH and —COOH, were considered. 1) These functional groups increase the ionic conductivity by facilitating the transfer of $Li^+$ ions between adjacent polar functional groups.[55–57] 2) They enhance adhesion between active materials and the current collector by forming strong hydrogen bonds.[72,73] 3) Binders with functional groups can provide robust electrostatic forces and form durable intramolecular interactions with neighboring polymer chains, acting as mechanical net points. This effect facilitates the diffusion of $Li^+$ ions within the ionomer by reducing the $Li^+$ transport distance.[74] Therefore, promising binder additives with polar functional groups were selected, including poly(acrylic acid) (PAA),[75–77] sodium


© 2025 The Author(s). Advanced Materials published by Wiley-VCH GmbH

15214095, 2025, 12, Downloaded from https://advanced.onlinelibrary.wiley.com/doi/10.1002/adma.202416872 by Chung-Ang University, Seoul, Wiley Online Library on [23/10/2025]. See the Terms and Conditions (https://onlinelibrary.wiley.com/terms-and-conditions) on Wiley Online Library for rules of use; OA articles are governed by the applicable Creative Commons License

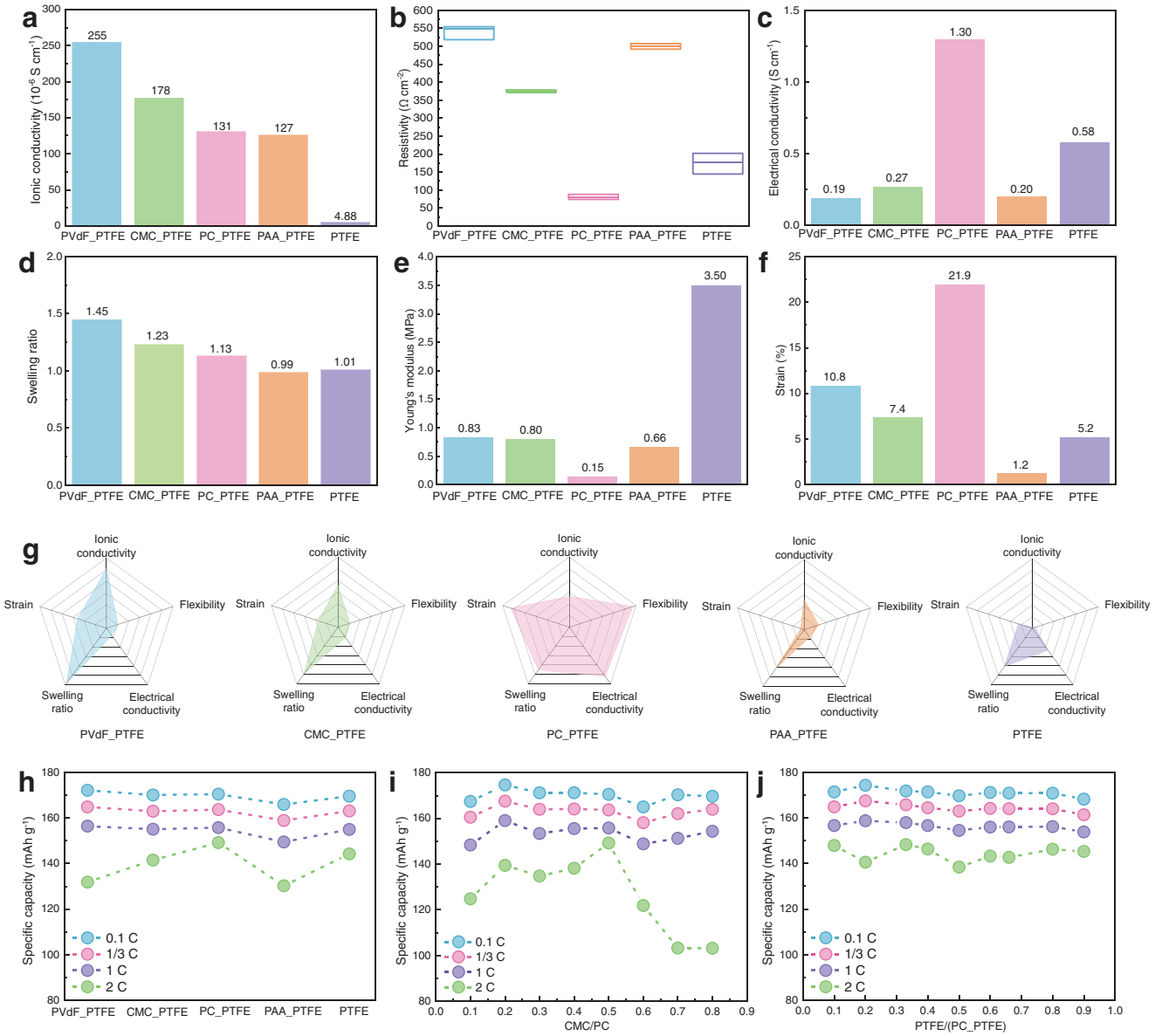



**Figure 3.** Performances of different properties were conducted to identify the optimal additive binder for the dry process. PVdF_PTFE (blue), CMC_PTFE (green), PC_PTFE (pink), PAA_PTFE (orange), and PTFE (purple) were compared. a) Ionic conductivity, b) resistivity, c) electrical conductivity, d) Swelling ratio, e) Young's modulus, and f) Strain (%) of each binder additive sheet formulated with PTFE. g) Radar chart summarizing the overall performance of binders across key parameters, as derived from the evaluations in (a–f). h) Specific capacity of the sheet-type cathodes with different binder additives. i) Rate performances for varying CMC:PC ratios. j) Rate capabilities based on varying PC:PTFE ratios at various C-rates (0.1 C, 1/3 C, 1 C, and 2 C).

carboxymethyl cellulose (Na-CMC),[78,79] and poly(acrylic acid)-grafted sodium carboxymethyl cellulose (PAA-CMC).[80,81]

The ionic conductivity of the binder influences the performance of the thick electrode. To study the interactions between the binder additives and PTFE, binder films were fabricated by mixing the binder additives and PTFE in a 1:1 weight ratio, which is essential for forming a sheet electrode. The ionic conductivity of each binder film was investigated using the bulk resistance from electrochemical impedance spectroscopy (EIS) spectra (Figure S3, Supporting Information). The ionic conductivity of the PTFE binder was $4.88 \times 10^{-6}$ S cm$^{-1}$, which was lower than that of the other binders (**Figure 3a**). With the introduction of the binder additives, the conductivity of the binder films increased. The ionic conductivities of the PVdF_PTFE, CMC_PTFE, PAA-CMC(PC)_PTFE, and PAA_PTFE samples were $2.55 \times 10^{-4}$, $1.78 \times 10^{-4}$, $1.31 \times 10^{-4}$, and $1.27 \times 10^{-4}$ S cm$^{-1}$, respectively. The ionic conductivity exhibited by the PVdF_PTFE binder was higher than those of the other binders.

The electrical conductivity of each cathode was evaluated using a 4-probe measurement. Due to the inherent insulating nature of binders, the electrical conductivity of the cathode was evaluated after the integration of each binder. Each cathode was mixed with the binder additives and PTFE in a 1:1 weight ratio. The average sheet resistance of PVdF_PTFE, CMC_PTFE, PC_PTFE,


© 2025 The Author(s). Advanced Materials published by Wiley-VCH GmbH

15214095, 2025, 12, Downloaded from https://advanced.onlinelibrary.wiley.com/doi/10.1002/adma.202416872 by Chung-Ang University, Seoul, Wiley Online Library on [23/10/2025]. See the Terms and Conditions (https://onlinelibrary.wiley.com/terms-and-conditions) on Wiley Online Library for rules of use; OA articles are governed by the applicable Creative Commons License

PAA_PTFE, and PTFE were 540.1, 374.6, 77.2, 494.0, and 173.8 Ω $cm^{-2}$, respectively (Figure 3b). The sheet resistances of all cathodes fabricated using the dry process were lower than those of the cathodes fabricated using the wet process with PVdF (2259.3 Ω $cm^{-2}$, Figure S4a, Supporting Information). Using these sheet resistance measurements, the electronic conductivity for each cathode was determined. The cathode with PC_PTFE binder exhibited the highest electrical conductivity (1.30 S $cm^{-1}$), while PVdF_PTFE, CMC_PTFE, PAA_PTFE, and PTFE exhibited values of 0.19, 0.27, 0.20, and 0.58 S $cm^{-1}$, respectively (Figure 3c). These values were higher than observed for the wet process PVdF cathode (0.04 S $cm^{-1}$, Figure S4b, Supporting Information). The improved electrical conductivity of the cathode using the PC-PTFE binder is attributed to its ability to maintain a uniform distribution of electrode particles and form a three-dimensional network structure. This network increases the direct contact area between electrode materials, optimizes conductive pathways and facilitates more efficient electron transport between the electrode particles.

The extent of volume expansion depends significantly on the properties of the binders. During the charge/discharge cycles, active particles cause only 4% of volume expansion, whereas the binders can expand by >50%.[82] The increased expansion weakens the adhesive force during cell operation and expels the electrolytes in the electrodes. This results in the destruction of the conductive network, which causes a loss of cycling performance.[83,84] However, low swelling prevents $Li^+$ ions from accessing different regions of the electrode composite, increasing electrical resistance. Therefore, moderate swelling values are preferred to facilitate $Li^+$ ion transport within the conductive carbon and binder.[85] A swelling test was performed to identify the optimal binder additive for the sheet-type electrode. The variation in swelling conditions is shown in Figure S5 (Supporting Information). The swelling ratios of each binder film after soaking in the electrolyte for 120 h is shown in Figure 3d. After 120 h, the PVdF_PTFE, CMC_PTFE, PC_PTFE, PAA_PTFE, and PTFE films expanded by 1.45-, 1.23-, 1.13-, 0.99-, and 1.01-fold, respectively. PC_PTFE was likely an adaptive binder additive with a moderate swelling ratio.

The mechanical properties of the binder film, which were identified using a universal testing machine (UTM), are shown in Figure 3e,f. The synergistic effect of the binder additive and PTFE was investigated via tensile tests. When the PTFE and binder additives were mixed, some films were reinforced for flexibility and strength. The PC_PTFE film experienced breakage until 21.9% strain owing to the soft PC binders, whereas PTFE resisted a lower strain of 6.0%. A significant synergistic effect was observed on the mechanical properties of the binders between PTFE and the soft PC. As summarized in Figure 3g, PC_PTFE showed the best performance among the binders for sheet-type electrodes, owing to its 1) high ionic and electrical conductivity, 2) moderate swelling, and 3) elastomeric properties.

The adhesion performance of the binder additives on the NMC 622 cathode was quantitatively evaluated via a 180° peel-off test using a UTM. Fabricated electrodes of equal thickness were prepared as rectangular shapes and attached to the 3 M tape (12 mm width). The adhesive force was measured by pulling the tape at a constant displacement rate (6 mm $min^{-1}$). The optical images obtained after the peeling test indicated that there were differences among the electrodes (Figure S6a, Supporting Information). In addition to a moderate swelling ratio, PC_PTFE exhibited a stronger adhesive force (0.9615 N $cm^{-1}$) with the Al current collector than that of PTFE (0.5733 N $cm^{-1}$) (Figure S6b, Supporting Information). This result highlighted the structural characteristics of the three-dimensional interconnected network of the PC binder. PTFE exhibited weak van der Waals forces owing to C—F bonds.[28–30] The PC binder was synthesized through a dehydration-condensation reaction, resulting in a crosslinked mesh structure.[80]

Half-cells consisting of a binder additive-incorporated composite cathode and a Li metal counter electrode were assembled to evaluate the effects of the binder additives on the electrochemical performance. The composite cathode contained NMC 622 ($LiNi_{0.6}Mn_{0.2}Co_{0.2}O_2$)/Super P/PTFE/binder additive (93:5:1:1 by weight) on an Al current collector. The effects of various binder additives on the rate performance (under a fixed areal mass loading of 18 mg $cm^{-2}$) were evaluated at dynamic C-rates of 0.1 C, 1/3 C, 1 C, and 2 C (Figure 3h; Figure S7, Supporting Information). The specific discharge capacities of the different binder additive-incorporated composite cathodes exhibited similar values, even at 1 C. The specific discharge capacities at 2 C of the PVdF_PTFE, CMC_PTFE, PC_PTFE, PAA_PTFE, and normal PTFE cathodes were 131.83, 141.52, 149.22, 130.22, and 144.26 mAh $g^{-1}$, respectively. The cathode with PC_PTFE exhibited a higher discharge capacity at 2 C than that of the other cathodes. The rate capability followed the same trend as that of the adhesive strength, which showed that the mechanical robustness of the electrode was a key factor affecting cycling performance.

To identify the optimal composition point of the PC, cathodes with identical active loadings were prepared with varying PAA:CMC weight ratios—9:1, 8:2, 7:3, 6:4, 5:5, 4:6, and 3:7—denoted as PC91, PC82, PC73, PC64, PC55, PC46, and PC37, respectively. After graft polymerization and the crosslinking reaction, the intensity of the sharp peak at ≈1690 $cm^{-1}$ was substantially reduced depending on the binder ratio (Figure S8, Supporting Information). This peak corresponded to the carboxylic group (—COOH) of PAA.[81] The effect of PC ratio on the rate performance was evaluated using a PC:PTFE ratio of 1:1 at the same C-rate. At a high current rate (2 C), the PC55_PTFE cells delivered 149.2 mAh $g^{-1}$ (Figure 3i). Among the various mixing ratios of PAA to CMC, the PC55 cell was selected as the optimal point (subsequently referred to as PC) because it exhibited the highest capacity retention (87.5%) at 2 C (Figure S9, Supporting Information).

The performance of PC electrodes prepared using varying PTFE ratios was investigated. The PC:PTFE ratio was set to 9:1, 8:2, 7:3, 6:4, 5:5, 4:6, 3:7, 2:8, and 1:9, and the corresponding samples were labeled PC_PTFE91, PC_PTFE82, PC_PTFE73, PC_PTFE64, PC_PTFE55, PC_PTFE46, PC_PTFE37, PC_PTFE28, and PC_PTFE19, respectively (Figure 3i). Some disadvantages were observed when the PTFE binder was incorporated in the DBE process: 1) precise control was required (as already observed in Figure 2; Figures S1 and S2, Supporting Information), and 2) binder decomposition[86] (additional explanation, see Figure S28, Supporting Information). The process sensitivity of DBE was mainly caused by PTFE fibrillation. PTFE fibrillation is essential for the dough of the dry electrode; however, fibrillation occurs even at low shear forces.[87–89] Therefore,


© 2025 The Author(s). Advanced Materials published by Wiley-VCH GmbH

15214095, 2025, 12, Downloaded from https://advanced.onlinelibrary.wiley.com/doi/10.1002/adma.202416872 by Chung-Ang University, Seoul, Wiley Online Library on [23/10/2025]. See the Terms and Conditions (https://onlinelibrary.wiley.com/terms-and-conditions) on Wiley Online Library for rules of use; OA articles are governed by the applicable Creative Commons License

the PTFE binder undergoes excessive fibrillation when mixing is not stringently controlled, complicating the production of free-standing electrodes.[90] To prevent challenges when mixing and binder decomposition during subsequential cycling, the binder additive ratio was increased. The PC_PTFE91 cell exhibited a high capacity (147.9 mAh $g^{-1}$ at 2 C); however, the fabrication of a dough-type electrode was challenging owing to the low quantity of PTFE binder (Figure S10, Supporting Information). Compared with the other electrodes composed of varying binder contents, the cathode with the PC_PTFE73 binder exhibited the highest capacity (148.3 mAh $g^{-1}$ at 2 C) and was a stable dough-type electrode (Figure 3j).

### 2.3. Elucidating the Role of the PC Binder

The properties of polymers are highly dependent on their structure. The chemistry and connections of the polymer chain create an internal entropy, which affects the entire system. Molecular dynamics simulations are used to estimate this internal entropy. The polymer structures and morphologies are analyzed before the construction of atomic scale electrode systems. The PC binder was synthesized, and its structure characterized using Fourier transform infrared (FTIR) spectroscopy. In addition to FTIR, X-ray photoelectron spectroscopy (XPS) and X-ray diffraction (XRD) analyses were performed to identify the structural changes in PC after the condensation reaction (Figures S11 and S12, Supporting Information). XPS C 1s spectra of PC showed peaks at 284.1, 285.7, 287.2, and 288.1, corresponding to C—C, C—O, COO—, and COOH, respectively, confirming the formation of ester bonds within PC. Additionally, XRD analysis revealed noticeable changes in the peak at 20°, indicating a reduction in crystallinity after polymerization. Electrode materials were not used in the preparation of the PAA, CMC, and PC polymer films (**Figure** 4a). Every polymer exhibited a —CH stretch band and a broad band for the —OH stretch band in the range of 2500–3700 $cm^{-1}$. The C═O carboxylic acid stretch in PAA was observed as an intense band at 1710 $cm^{-1}$. The CMC exhibited two main peaks at 1590 and 1021 $cm^{-1}$, which were assigned to the carboxylate (COO–) and ether (C–O–C) stretch bands. The main peaks of PAA and CMC were retained in the PC spectrum, highlighting the condensation reaction between PAA and CMC (Figure 4b).[84,91] The corresponding peaks were verified by using the density functional theory to calculate the IR spectra. The CMC monomer, PAA dimer, and PAA dimer grafted CMC monomer (PC) were used in the calculation (Figure S13, Supporting Information). The PC binder was uniformly attached to the NMC particles after it was ground in a ball mill (Figure 4c; Figure S14, Supporting Information). EDS analysis showed that Na elements remained within the molecular structure of PC and were evenly distributed on the surface of NMC. When only PTFE is present, the fibrous PTFE chain adheres to the NMC surface, but it binds the particles together solely through PTFE's adhesive force, without anchoring to specific areas (Figure 1b,e,g). In contrast, when PTFE is additionally mixed with the PC binder, the fibrous PTFE chain entangles around the PC which work as bollard, securing and holding the individual particles (Figure 1c,f,h).

Two types of electrode systems were constructed: 1) NMC with a PTFE binder only, and 2) NMC with a PC_PTFE binder. To investigate the impact of the PC binder on the electrode with PTFE, all other settings remained identical except for the presence of the PC binder in the second system. First, the optimal adsorption point of the PC binder on the NMC surface was identified using machine learning potential based density functional theory calculations. Following the construction of the NMC surface model, the PC molecule was rotated through 15 different configurations, and the corresponding adsorption energies were calculated. The adsorption states were classified into three primary categories: 1) two Na atoms from PC adsorbed onto the O atoms of the NMC surface (referred to as PC_2Na), 2) one Na atom adsorbed (PC_1Na), and 3) long distance interactions between the surface and functional groups (–OH, –COOH) of PC instead of Na atoms (PC_0Na). The inset images in Figure 4e show the representative images of each adsorption state. The average adsorption energy values for each of the corresponding adsorption states were calculated and used for further analysis (Figure S15, Supporting Information). A strong interaction between Na from PC and O from NMC were observed using computational analysis. When two Na atoms participated in the bonding, the average adsorption energy was ≈−2.24 eV, indicating robust adsorption. The involvement of only one Na atom resulted in an adsorption energy of ≈−1.12 eV, approximately half the value observed for two Na atoms. In cases where the interactions involved —OH and —COOH functional groups rather than Na atoms, the adsorption energies were significantly lower (−0.37 eV), which were attributed to the stabilization energy from long-range dipole-dipole interactions. The substantial variance observed when the –COOH functional group participated in the interaction was attributed to differences in the number of functional groups participating in the interactions. PTFE exhibited the highest adsorption energy (−0.09 eV) because of the electrostatic repulsion between O from NMC and F from PTFE. This results in their inherently low adsorption (Figure 4c).

NVT-MD simulations were performed using the Langevin heat bath method for 10 ps after reaching 400 K.[92,93] To guarantee sufficient binder dynamics, MD was performed at high temperatures. The binder gradually detached from the electrode surface over time after reaching 400 K in the system only containing the PTFE binder (Figure 4d; Figure S16a, Supporting Information). The average distance of the F atoms in PTFE near the surface was calculated over time, showing a sharp increase from an initial 4.2 Å to 6.6 Å (Figure 4f). In contrast, in the PC_2Na system, the PC binder physically held the PTFE in place, preventing it from detaching from the surface (Figure 4e; Figure S16b, Supporting Information). Additionally, the structure of the PC binder did not collapse or decompose. This was likely due to the mitigation of the structural strain or stress by the migration of the adsorbed Na atoms across the O layer of the electrode surface (Movies S1–S3, Supporting Information). The free Na site in the PC_1Na system strongly interacted with the F atoms of the detached PTFE (Red arrow in Figure S16c,d, Supporting Information). The interaction energy between Na and F was −0.35 eV, which was a 2 to 4.5 times stronger interaction than that of the interaction between PTFE and the NMC surface. Furthermore, when a large number of Na—F bonds are formed, the electrochemical stress applied to the system is likely to be distributed across the entire bonding network. This


© 2025 The Author(s). Advanced Materials published by Wiley-VCH GmbH

15214095, 2025, 12, Downloaded from https://advanced.onlinelibrary.wiley.com/doi/10.1002/adma.202416872 by Chung-Ang University, Seoul, Wiley Online Library on [23/10/2025]. See the Terms and Conditions (https://onlinelibrary.wiley.com/terms-and-conditions) on Wiley Online Library for rules of use; OA articles are governed by the applicable Creative Commons License

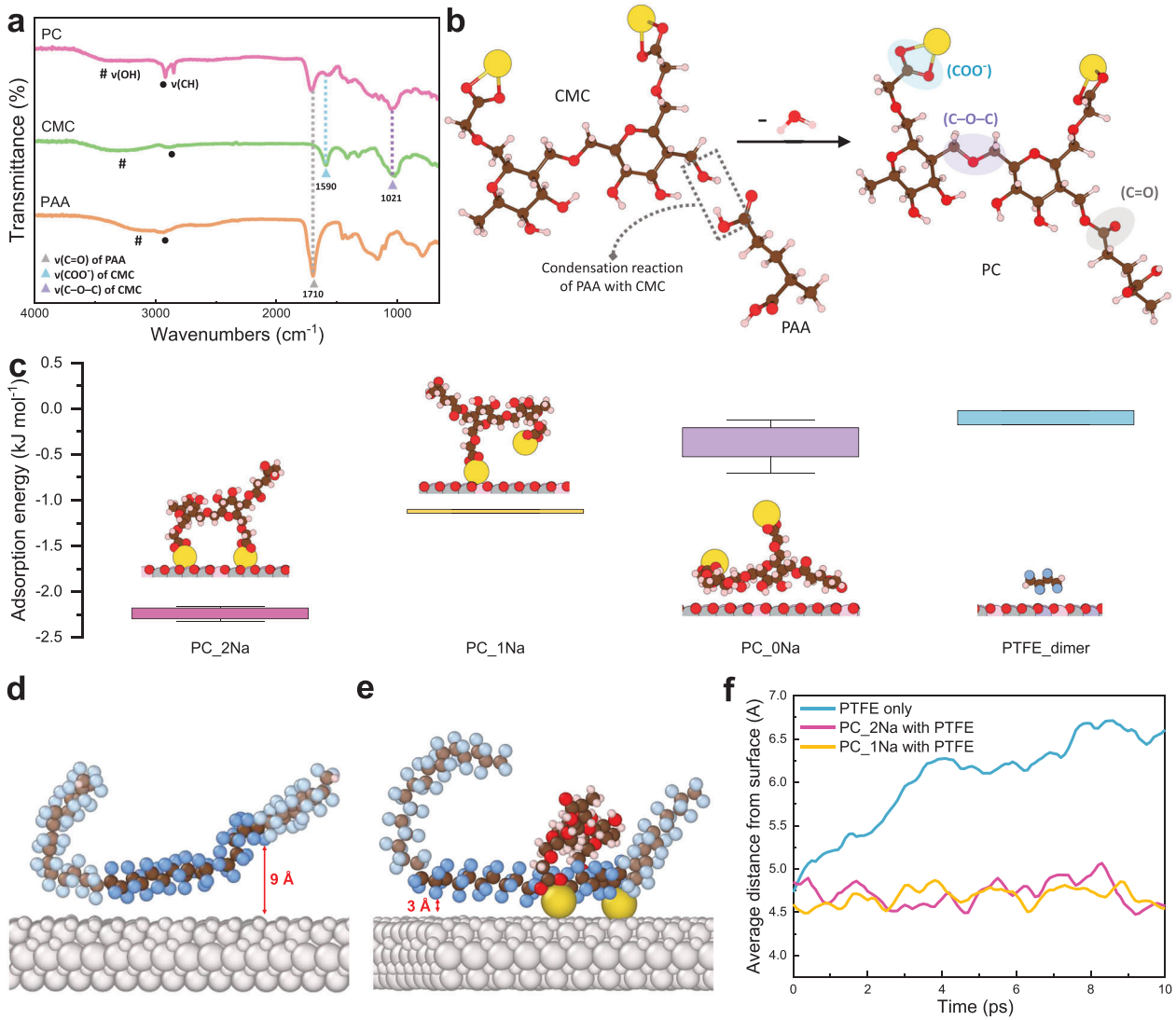



**Figure 4.** a) FTIR spectra of binder powders (PAA, CMC, and PC). b) schematic of the PC formation (carbon: dark brown, hydrogen: pale pink, oxygen: red, sodium: yellow). c) Adsorption energy of PC monomers and PTFE dimers on the NMC surface (carbon: dark brown, hydrogen: pale pink, oxygen: red, sodium: yellow, fluorine: blue, nickel: gray, manganese: pink); d) PTFE, and e) PC_2Na with PTFE on the NMC surface after running MD simulations at 400 K for 10 ps. The same length of the PTFE binder was used in both calculations (carbon: dark brown, hydrogen: pale pink, oxygen: red, sodium: yellow, NMC surface: light gray). f) Average change in distance of the PTFE binder with and without PC on the NMC surface. For distance calculation, the C and F atoms in dark brown and blue from (d) and (e) were only considered.

increases the total energy required to weaken or disrupt the PTFE-PC binding network. Experimentally, the Na-F interaction was verified through XPS analysis (see Note S3 and Figure S17, Supporting Information), where distinct peaks corresponding to Na—F bonding were observed. Furthermore, the deconvolution of the F 1s peak revealed that the peak area corresponding to Na—F bonds is larger than that of C—F bonds. Based on this result, it can be argued that the abundant chemical interactions involving Na—F bonds contribute to strengthening the PTFE's adhesion within the PC network. This interaction helped stabilize the PTFE within the structure through chemical interactions. As shown in Figure 4f, the PTFE did not completely detach in both systems (PC_2Na and PC_1Na with PTFE); however, its distance fluctuated between 4.5 and 4.9 Å. The PAA polymer formed a branched structure with the PC binder after grafting. This branching physically entangled PTFE with the PAA branches. This indicates that the PC binder behaved as the "bollards", physically and chemically anchoring PTFE, thereby preventing its detachment from the surface. This resulted in the high mechanical resistance to strain of PC_PTFE observed in the experimental results (Figure 3e,f).

### 2.4. Morphological Analysis to Compare the Effects of Different Binders on Porosity

The morphological characteristics of each binder in the high-loading electrode were measured (Figure S18, Supporting


© 2025 The Author(s). Advanced Materials published by Wiley-VCH GmbH

15214095, 2025, 12, Downloaded from https://advanced.onlinelibrary.wiley.com/doi/10.1002/adma.202416872 by Chung-Ang University, Seoul, Wiley Online Library on [23/10/2025]. See the Terms and Conditions (https://onlinelibrary.wiley.com/terms-and-conditions) on Wiley Online Library for rules of use; OA articles are governed by the applicable Creative Commons License

Information) by examining their cross-sections. A previous study showed that the PVdF electrode exhibited mechanical cracks and separation from the substrate, which occurred during nonuniform binder mixing, solvent evaporation, and compression at high loading (Figure S19, Supporting Information).[94] The mechanical cracks rendered parts of the material inactive with insufficient conductive pathways, which reduced the reaction surface area and complicated the $Li^+$ ion diffusion pathway. Consequently, capacity loss occurred, and the severity of performance degradation was higher at higher C-rates. In contrast, the PTFE and PC_PTFE73 electrodes were dense, and exhibited favorable adhesion to the substrate and uniform binder dispersion, as indicated by energy-dispersive X-ray spectroscopy (EDS) mapping data. The results indicate that the dry electrode process was more suitable for manufacturing high-loading electrodes than that of the wet film process. The dispersion of NMC 622, Super P, and the binder was assessed using a 3D X-ray tomography microscope (XRM) system (Figure S20, Supporting Information). When X-rays were used for tomography characterization, the conductive carbon and binder components were transparent; therefore, the NMC 622 particles were only discernible in Figure S20a,d (Supporting Information). The cyan areas represent the conductive carbon and binder components (Figure S20b,e, Supporting Information). The optimized drying process was achieved uniform dispersion even under high-loading conditions, as confirmed by the XRM results of the PC_PTFE cathode (30 mg $cm^{-2}$) and PVdF-based wet cathode (15 mg $cm^{-2}$) (Figure S20c,f, Supporting Information). However, differences in porosity were observed between the two electrodes. Although both electrodes had the same density of 3.0 g $cm^{-3}$, differences in the tap density of the binders influenced the calculated porosity values. The PC_PTFE73 electrode exhibited 25.9% higher porosity than that of the PVdF wet electrode (17.7%) (refer to Table S3, Supporting Information for details). Higher porosity could be achieved within the same electrode density due to the structure of the binder. Furthermore, the tortuosity of each cathode was calculated based on cross-sectional SEM images. The tortuosity of the PC_PTFE73-based cathode was 1.30, whereas that of the PTFE-based cathode was 1.40. These characteristics are advantageous in high-loading thick electrodes. As the electrode thickness increases, the distance electrons must travel from the current collector to the active material becomes longer, and the diffusion distance for Li-ions through the electrode pores also increases.[95–97] This results in poor transport characteristics and slow reaction kinetics. The high porosity of the PC_PTFE73-based cathode improves the contact area between the electrolyte and the active material, effectively reducing the lithium-ion diffusion distance. Its low tortuosity further shortens the electron transport pathways.[98,99] Consequently, the PC_PTFE73-based cathode positively influenced electrolyte conductivity, lithium diffusion coefficient enhancement and high electrical conductivity due to its higher porosity and lower tortuosity.

### 2.5. Enhanced High-Loading Cathode Performance with the PC_PTFE73 Binder

The effect of the binder in the electrochemical evaluations was observed when the areal active-material loading was increased to 30 mg $cm^{-2}$. A comparison of the electrochemical characteristics of NMC 622 cathode via the dry and the conventional slurry-cast electrode (PVdF) was performed. The galvanostatic charge/discharge (GCD) profiles at 0.1 C and 2 C are shown in **Figure 5a,b**, respectively. The galvanostatic curves followed similar trends at 0.1 C (Figure 5a); however, the increase in the overpotentials of the PVdF and PTFE electrodes was higher than that of the overpotential of the PC_PTFE electrode at 2 C (Figure 5b), indicating that the interfacial resistance of the electrode comprising PC_PTFE was lower than those of the other electrodes. The lower capacities of the PVdF and PTFE electrodes can be explained by the increased IR drops. Consequently, the PC_PTFE73 electrode with a relatively lower overpotential exhibited an improved rate capability (Figure 5c). In particular, the PC_PTFE73 electrode exhibited a specific discharge capacity of 168.5 mAh $g^{-1}$ (5.0 mAh $cm^{-2}$) at 1/3 C, which was higher than that of the PVdF electrode. At 1 C, PC_PTFE73 delivered a specific discharge capacity of 159.5 mAh $g^{-1}$ (4.8 mAh $cm^{-2}$), outperforming the PTFE and PVdF electrodes. The disparity in discharge capacity was observed at 2 C, with the PC_PTFE73, PTFE, and PVdF electrodes exhibiting 133.2 mAh $g^{-1}$ (4.0 mAh $cm^{-2}$), 108.1 mAh $g^{-1}$ (3.2 mAh $cm^{-2}$), and 76.5 mAh $g^{-1}$ (2.3 mAh $cm^{-2}$), respectively.

The long-term cycling performance was evaluated using a GCD test at a mass loading of 25 mg $cm^{-2}$ (Figure 5d). PC_PTFE73 exhibited a capacity of 139.2 mAh $g^{-1}$ after 100 cycles at 1/3 C, retaining 83% of its initial capacity. In contrast, the PTFE-dried film (84.0 mAh $g^{-1}$) and PVdF wet electrodes (77.6 mAh $g^{-1}$) exhibited lower capacities after 100 cycles, corresponding to capacity retentions of 51% and 47%, respectively. The PTFE and PVdF electrodes underwent rapid capacity decay after ≈70 cycles which was caused by increased resistance due to charge transfer and lithium-ion diffusion limitations in thick electrodes. Compared to regions near the electrolyte, the regions closer to the current collector become less active in the reaction, resulting in selective reactions. Consequently, only certain regions of active materials continue to react, accelerating degradation.[68,70,100–103] The PC_PTFE73-based cathode demonstrated higher porosity and lower tortuosity at the same loading and density compared to electrodes using other binders. (Table S3, Supporting Information) This higher porosity facilitates easier penetration of the electrolyte into the electrode, reducing lithium diffusion distances, while the lower tortuosity shortens the electron transport pathways within the electrode.[99,104] These characteristics prevent degradation in thick electrodes, distinguishing the PC_PTFE73 cathode from the others.

To further understand the difference in cycling stability, the electrode morphology after 100 cycles using FE-SEM (Figure S21, Supporting Information). The FE-SEM images revealed distinct differences in the cathode depending on the binder. The cathode with the PC_PTFE73 binder (Figure S21a, Supporting Information) exhibited a smoother and uniform surface without visible cracks in the NMC particles, indicating enhanced structural stability. In contrast, the cathode with the PTFE binder (Figure S21b, Supporting Information) showed secondary NMC particles fractured into smaller parts (remarked with white circles), demonstrating poor structural stability after cycling. The structural changes in the cathodes after 100 cycles were further examined using XRD analysis (Figure S22, Supporting Information). These results indicate that the PC_PTFE73 binder played a


© 2025 The Author(s). Advanced Materials published by Wiley-VCH GmbH

15214095, 2025, 12, Downloaded from https://advanced.onlinelibrary.wiley.com/doi/10.1002/adma.202416872 by Chung-Ang University, Seoul, Wiley Online Library on [23/10/2025]. See the Terms and Conditions (https://onlinelibrary.wiley.com/terms-and-conditions) on Wiley Online Library for rules of use; OA articles are governed by the applicable Creative Commons License

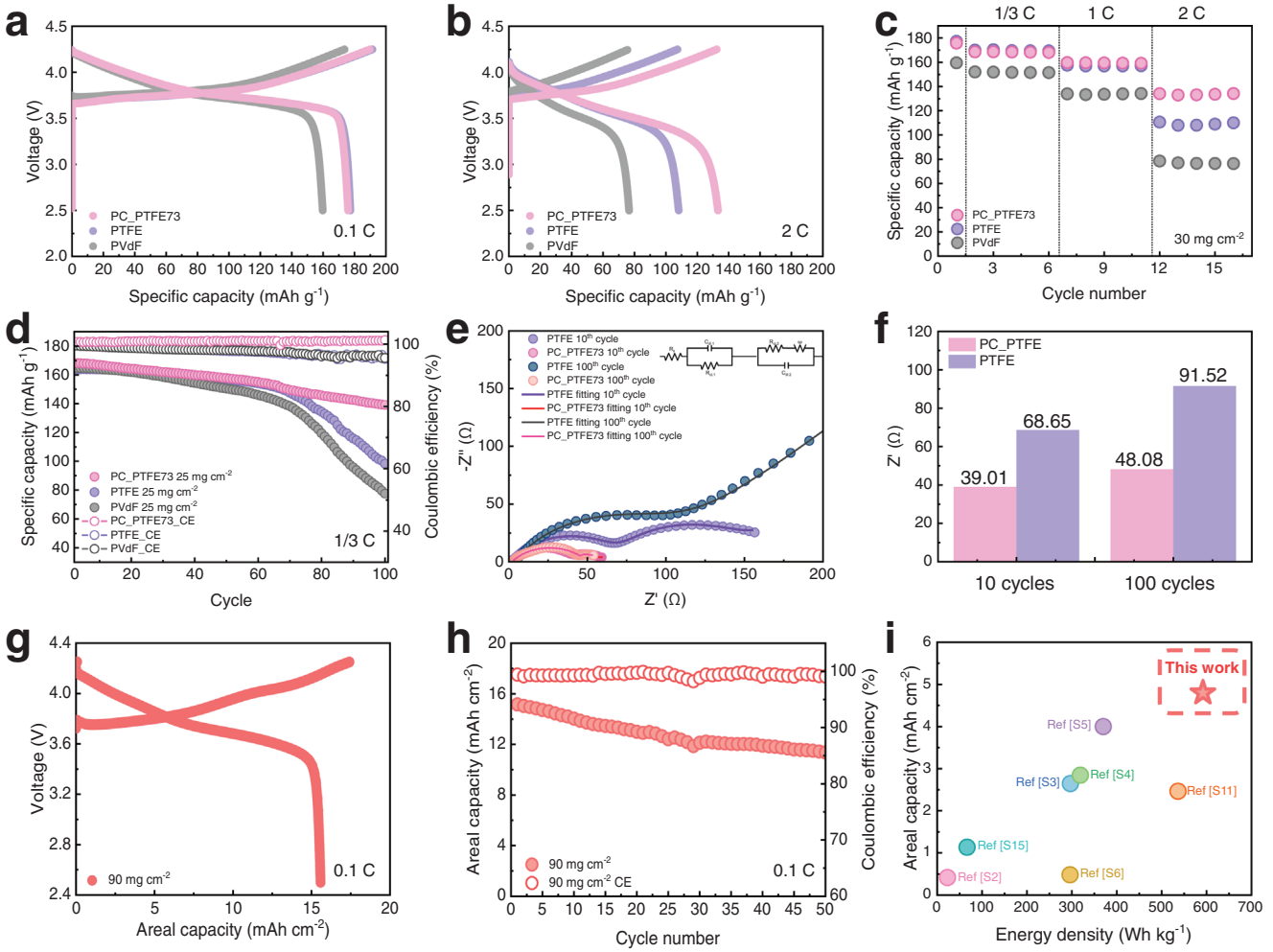



**Figure 5.** Galvanostatic charge/discharge profiles of different binders between 2.5 and 4.25 V at a) 0.1 C and b) 2 C. c) Rate capability at rates ranging from 0.1 C to 2 C for a 30 mg $cm^{-2}$ electrode. d) Cycle performance of each binder at 1/3 C for a 25 mg $cm^{-2}$. e) Nyquist plot and corresponding fitted lines for the PTFE and PC_PTFE electrodes after 10 cycles and 100 cycles. f) Changes in the interfacial resistances of PC_PTFE and PTFE during cycling. g) Galvanostatic charge/discharge profiles of ultra-high loading (90 mg $cm^{-2}$) at 0.1 C. h) Cycle performance of 90 mg $cm^{-2}$ at 0.1 C. i) Performance of the areal density and energy density of this study and previous studies on the DBE cathode half-cell at 1 C.

critical role in improving the structural stability and electrochemical performance of the electrode. This improved performance may have occurred because of the synergistic effect of the PC binder and the introduction of the PTFE binder. The synergistic effect enhanced ionic conductivity and adhesive force. The stable performance of the PC_PTFE73 binder in NMC electrodes suggests its potential for high-voltage systems, such as $LiMn_{1.5}Ni_{0.5}O_4$ cathodes operating at 4.9 V. CV and LSV analysis from 2.5 V to 5.0 V showed that, the binder maintained stability (Figure S23, Supporting Information). This indicates the binder's suitability for both NMC and future high-voltage cathode materials.[105–107]

EIS measurements were performed on the NMC-Li asymmetric configurations after 10 and 100 cycles to assess the distinct cycling performance (Figure 5e; Figure S24, Supporting Information). The semicircle observed in the mid to low-frequency ($10^1$–$10^4$ Hz) represents the interfacial resistance, which is the resistance encountered at the electrode/electrolyte interface and primarily includes the charge transfer resistance ($R_{ct}$).[108,109] After ten cycles, the electrodes using the PC_PTFE73 binder exhibited an interfacial resistance of 39.01 Ω, which was 1.76 times lower than that of the electrodes using PTFE (68.65 Ω). After 100 cycles, the interfacial resistance of PC_PTFE73 increased to 48.08 Ω, whereas that of PTFE increased to 91.52 Ω (Figure 5f). The lower increase in the interfacial resistance of PC_PTFE73 was attributed to the effect of PC_PTFE, which comprised a net-like structure. This resulted in the enhancement of particle-to-particle cohesion and electrode-to-current collector adhesion, as well as interfacial properties. The effect of PC_PTFE was confirmed by the Li ion diffusion coefficient ($D_{Li+}$) of each electrode, which was measured after 10 cycles (Figure S25, Supporting Information). After 10 cycles, the $D_{Li+}$ of PC_PTFE73 was 5.09 $e^{-14}$ $m^2$ $s^{-1}$, which was 20 times higher than that of the electrode using PTFE (2.53 $e^{-15}$ $m^2$ $s^{-1}$).

The cycling performance of the PC_PTFE73 cells comprising various mass loadings was assessed (Figure S26, Supporting


© 2025 The Author(s). Advanced Materials published by Wiley-VCH GmbH

15214095, 2025, 12, Downloaded from https://advanced.onlinelibrary.wiley.com/doi/10.1002/adma.202416872 by Chung-Ang University, Seoul, Wiley Online Library on [23/10/2025]. See the Terms and Conditions (https://onlinelibrary.wiley.com/terms-and-conditions) on Wiley Online Library for rules of use; OA articles are governed by the applicable Creative Commons License

Information). Complementary studies were conducted to evaluate the cell performance of PC_PTFE73 when the cathode loading exceeded 30 mg $cm^{-2}$ (Figure S27, Supporting Information). Reasonable gravimetric performances were observed. To assess the performance under ultrahigh loading conditions, the cycling stability of the electrode was evaluated at 90 mg $cm^{-2}$ (Figure 5g,h). The electrode exhibited 15.6 mAh $cm^{-2}$ and its operation was stable over 50 cycles. The use of the PC_PTFE73 binder enables the fabrication of cathodes under ultrahigh loading conditions while maintaining satisfactory performance.

The capacity density of the PC_PTFE73 electrode was superior to that observed in previous studies (Tables S1 and S2, Supporting Information). Regarding DBE, previous studies utilizing active materials with high Ni contents or special conductive materials have shown higher areal capacities and energy densities at 0.1 C. However, exponential degradations in capacity were observed at C-rates of 1 C in these studies; additionally, the values were significantly lower at 2 C. Compared with high-loading wet processes, conventional wet processes did not exceed 50 mg $cm^{-2}$ and exhibited lower energy density values at higher C-rates under the same loading conditions. However, a significant quantity of capacity was maintained as the C-rate increased (1 C), representing the best performance among dry cathode and high-loading wet studies to date (Figure 5i).

### 2.6. Role of Binders in CEI Composition: XPS Analysis of PC_PTFE73 and PTFE Cathodes

To analyze the chemical composition of the outer cathode electrolyte interphase (CEI) species, the coin cells subjected to 100 cycles at 1 C were disassembled and analyzed using X-ray photoelectron spectroscopy (XPS) (Figure S28, Supporting Information). In addition, XPS depth profiling with different sputtering times (10, 20, 30 s) was further studied (Figures S29–S31, Supporting Information). It shows the C 1s, O 1s, and F 1s XPS profiles of the cathodes cycled with PC_PTFE73 and PTFE. Peaks corresponding to the C—C, C—O, C═O, $ROCO_2Li$, $Li_2CO_3$, and $CF_2$ bonds were observed in the C 1s spectra of the PC_PTFE73 and PTFE electrodes (Figures S28a,d and S29, Supporting Information). A lower intensity peak corresponding to the $CF_2$ bonds (291.7 eV) was observed for the cathode comprising PC_PTFE73 because of the reduced PTFE content. As the carbonate electrolyte solvent decomposed, the C—O and C═O peaks corresponded to $ROCO_2Li$ and $Li_2CO_3$, respectively.[27] Compared with the PTFE cathode, lower peak intensities of the C—O, C═O, and $ROCO_2Li$ bonds were observed for the PC_PTFE73 cathode, suggesting reduced carbonate solvent decomposition on the CEI film. The peaks at 533.5, 532.0, and 530.0 eV in the O 1s spectra were attributed to $ROCO_2Li$, $Li_2CO_3$, and M–O (M = Ni, Co, or Mn), respectively.[110] The intensity of the $ROCO_2Li$ peak on the PC_PTFE73 cathode surface was lower than that of PTFE, indicating that the PC binder suppressed the decomposition of carbonate solvents (Figures S28b,e, and S30, Supporting Information). In addition, the difference between the F 1s spectral peaks of PC_PTFE73 and PTFE in the CEI composite occurred because of the ratio of LiF (685.0 eV) to $Li_xPO_yF_z$ (687 eV).[111–113] The CEI of PC_PTFE73 comprised 29.8% LiF, whereas the PTFE exhibited a higher LiF content (37.4%) (Figure S28c,f, Supporting Information). The LiF formation on the cathode surface is known to enhance CEI stability and cyclability.[114–116] However, the increased LiF on the CEI of the PTFE cathode was attributed to the additional decomposition of the PTFE binder alongside the electrolyte during cycling. Tao et al. demonstrated that PTFE dissociates on the cathode side forming LiF in the presence of the $LiClO_4$ electrolyte, where PTFE is the only F source.[86] The decomposition of the binder results in challenges, such as reduced electrode integrity and increased resistance. Furthermore, XPS depth profiling revealed that the high LiF concentration on the surface drops significantly with depth for the PTFE cathode, indicating a non-uniform LiF distribution due to PTFE decomposition. In contrast, for PC_PTFE73 cathode, the change in LiF concentration with depth is less pronounced (Figure S31, Supporting Information). This result suggests that PC_PTFE73 cathode possess a more stable and uniform CEI interface.[117] Consequently, the decomposition of PTFE significantly reduces cycle stability and increases resistance compared with those of the PC_PTFE73 electrode (Figure 5d,f).

A solvent-free dry electrode process was used to fabricate coin-cell-type full cells for the evaluation of the potential utility of the PC_PTFE73 cathode in practical batteries. These full cells consisted of a NMC 622@PC_PTFE73 cathode and a Graphite@CMC wet process anode/ Graphite@PTFE dry process anode, respectively.[118] The performance details of the Graphite half-cells were delineated in Figure S32 (Supporting Information). The full cells were assessed between 2.5 and 4.25 V. The GCD profiles of the NMC 622@PC_PTFE73// Graphite@PTFE full cell from 1/3 C to 2 C at 25 °C are shown in Figure S33a (Supporting Information). The rate capability of the NMC 622@PC_PTFE73//Graphite@PTFE full cell is shown in Figure S33b (Supporting Information). The cell was cycled after one activation cycle at 0.1 C. The cell retained a discharge capacity of 119.8 mAh $g^{-1}$ after the C-rate was increased to 2 C. A capacity of 120.0 mAh $g^{-1}$ was maintained at 0.5 C when the full cell was subjected to 50 cycles, corresponding to a capacity retention of 84% (Figure S34, Supporting Information). At the Graphite@PTFE operational voltage, the low LUMO of PTFE resulted in susceptibility to binder degradation, resulting in decreased adhesion properties and exponential capacity reduction.[26,50] Therefore, further development of the anode binder is required for the enhancement of the cycling performance of larger cells. To eliminate the performance degradation caused by unstable anodes, other full cell tests were conducted using anodes manufactured through the conventional wet process. After 100 cycles, the full cell retained a capacity of 134.4 mAh $g^{-1}$ at 0.2 C, resulting in a capacity retention of 86% (Figure S35, Supporting Information). The issues associated with Graphite@PTFE were resolved, and the PC_PTFE73 binder performed effectively at the cathode. Therefore, the advantage of using the PC_PTFE73 binder on the NMC 622 cathode was demonstrated by its high-rate capability. Pouch cells were fabricated using PTFE and PC_PTFE73 binders, respectively (Figure S36a, Supporting Information). A commercial graphite electrode (density, 1.5 g $cm^{-3}$) was used as the anode. The pouch cell with the PC_PTFE73 binder achieved a higher areal capacity of 8 mAh $cm^{-2}$ at 0.5 C compared to the PTFE-based pouch cell, confirming that PC_PTFE73 operates effectively in pouch cell as well (Figure S36b,c, Supporting Information).


© 2025 The Author(s). Advanced Materials published by Wiley-VCH GmbH

15214095, 2025, 12, Downloaded from https://advanced.onlinelibrary.wiley.com/doi/10.1002/adma.202416872 by Chung-Ang University, Seoul, Wiley Online Library on [23/10/2025]. See the Terms and Conditions (https://onlinelibrary.wiley.com/terms-and-conditions) on Wiley Online Library for rules of use; OA articles are governed by the applicable Creative Commons License

## 3. Conclusion

Using an optimal solvent-free mixing process, a novel binder additive strategy for developing high-mass-loading cathodes without capacity loss that satisfy the following requirements was developed: 1) high ionic conductivity; 2) strong adhesion between the electrode and current collector; and 3) electrochemical stability at high voltages. Unlike PTFE alone, the PC_PTFE73 binder demonstrated an ability to enhance both ion conductivity and adhesion properties by acting as "bollards", physically and chemically anchoring PTFE to the electrode surface. The dry mixing process, under optimized mechanical conditions, eliminates the need for solvents, reducing environmental impact and simplifying the electrode manufacturing process. This makes it attractive for sustainable, cost-efficient production. However, scaling up this process presents challenges such as achieving uniform material distribution in large batches and controlling shear force to prevent excessive PTFE fibrillation. While laboratory-scale equipment may require significant adjustments for industrial use, ongoing advancements in mixing technologies offer promising solutions, and pursuing these advancements will be our future work. The PC binder, especially in the presence of Na atoms, forms strong interactions with NMC, stabilizing the system and preventing the detachment of PTFE, as evidenced by the deep-learning-based MD simulations. This behavior explains the superior mechanical resistance and strain tolerance of the PC_PTFE system observed in experiments. The battery performance of NMC 622 with the PC_PTFE73 binder was superior to that of PTFE, achieving 133.2 mAh $g^{-1}$ (4.0 mAh $cm^{-2}$) when tested at a high C-rate (2 C) and loading (30 mg $cm^{-2}$). Owing to its high ionic conductivity and stability at high voltages, the NMC 622 battery with PC_PTFE73 delivered a high capacity of 139.2 mAh $g^{-1}$ at 1/3 C with 83% retention after 100 cycles, which was significantly higher than that of the PTFE (84.0 mAh $g^{-1}$ and 51%) and PVdF (77.6 mAh $g^{-1}$ and 47%) cells. Even at ultra-high loading (90 mg $cm^{-2}$), the cathode exhibited a capacity of 15.6 mAh $cm^{-2}$. These performances were better than that of previous DBE methodologies using the same cathode. By partially replacing the PTFE binder with PC, LiF formation was mitigated owing to binder decomposition; additionally, the formation of a thick CEI layer was prevented, thereby reducing the rate of capacity reduction, even during long-term cycling.

A full cell was fabricated for the anode and cathode using a solvent-free process. This cell exhibited a high capacity (119.8 mAh $g^{-1}$ at 2 C) and maintained 84% capacity retention over 50 cycles (120.0 mAh $g^{-1}$ at 0.5 C). Upon addressing the limitations of PTFE at the anode, the capacity of the full cell was 134.4 mAh $g^{-1}$ at 0.2 C, which was retained at 86% after 100 cycles. The binder additive strategy for tailoring high ionic conductivity is likely universal and can be extended to other systems. This work represents a significant advancement in simplifying the fabrication of high-energy-density Li-ion batteries by eliminating the use of solvents with a binder design.

## Supporting Information

Supporting Information is available from the Wiley Online Library or from the author.

## Acknowledgements

This work was supported by the Hyundai NGV and Hyundai Motor Company, the National Research Foundation (NRF) grant funded by the Korea government (MSIT) (RS-2023-00280278), the Korea government (MSIT), under the ITRC support program (IITP-RS-2024-00436248) supervised by the IITP, the Commercialization Promotion Agency for R&D Outcomes (COMPA) funded by the Korea Government (MSIT) (2021-RMD-S05), the H2KOREA funded by the Korea Government (MOE) (2022Hydrogen fuel cell-003, Innovative Human Resources Development Project for Hydrogen Fuel Cells), and the National Institute of Supercomputing and Network/KISTI with supercomputing resources including technical support (KSC-2022-CRE-0061).

## Conflict of Interest

The authors declare no conflict of interest.

## Author Contributions

J.K., H.E., and S.J. contributed equally to this work. J.K., H.E., I.N., and H.S. conceived the ideas of this work. J.K., H.E., S.J., and M.-L.S. designed the experiments and simulations. J.K., H.E., and D.Y. fabricated the materials and the battery cells. J.K., H.E., S.J., H.L., and M.K. conducted the experimental analyses. J.K., H.E., and S.J. wrote the first draft of the paper. All authors contributed to the discussions of the results and the revision of the manuscript. J.W.H., I.N., and H.S. supervised the entire project.

## Data Availability Statement

The data that support the findings of this study are available from the corresponding author upon reasonable request.

## Keywords

bollard-anchored binder, dry electrode, high-loading cathode, PFAS-less binder, solvent-free process

Received: November 2, 2024
Revised: January 7, 2025
Published online: February 18, 2025

[1] P. Mitchell, L. Zhong, X. Xi, B. Zou, (Tesla Inc.), US Patent US20090239127A1, **2009**.
[2] P. Mitchell, X. Xi, L. Zhong, B. Zou, (Tesla Inc.), US Patent US20080102371A1, **2008**.
[3] P. Mitchell, X. Xi, B. Zou, L. Zhong, (Tesla Inc.), US Patent US20060137158A1, **2006**.
[4] E. Pameté, J. G. Ruthes, M. Hermesdorf, A. Seltmann, D. J. Tarimo, D. Leistenschneider, V. Presser, *Energy Environ. Mater.* **2025**, *8*, e12775.
[5] D. Cao, Y. Zhao, X. Sun, A. Natan, Y. Wang, P. Xiang, W. Wang, H. Zhu, *ACS Energy Lett.* **2020**, *5*, 3468.
[6] Y. Lu, C.-Z. Zhao, H. Yuan, J.-K. Hu, J.-Q. Huang, Q. Zhang, *Matter* **2022**, *5*, 876.
[7] J. H. Sung, T. W. Kim, H.-K. Kang, S. Y. Choi, F. Hasan, S. K. Mohanty, J. Kim, M. K. Srinivasa, H.-C. Shin, H. D. Yoo, *Korean J. Chem. Eng.* **2021**, *38*, 1059.
[8] H. S. Ko, H. W. Park, G. J. Kim, J. D. Lee, *Korean J. Chem. Eng.* **2019**, *36*, 620.


© 2025 The Author(s). Advanced Materials published by Wiley-VCH GmbH

15214095, 2025, 12, Downloaded from https://advanced.onlinelibrary.wiley.com/doi/10.1002/adma.202416872 by Chung-Ang University, Seoul, Wiley Online Library on [23/10/2025]. See the Terms and Conditions (https://onlinelibrary.wiley.com/terms-and-conditions) on Wiley Online Library for rules of use; OA articles are governed by the applicable Creative Commons License

[9] J. Sherwood, T. J. Farmer, J. H. Clark, *Chem* **2010**, *4*, 2018.
[10] J. Li, Y. Lu, T. Yang, D. Ge, D. L. Wood, Z. Li, *Iscience* **2020**, *23*, 101081.
[11] C. Chen, V. Reddy Tatagari, H. Lin, L. Shaw, *J. Energy Chem.* **2023**, *78*, 240.
[12] H.-H. Ryu, B. Namkoong, J.-H. Kim, I. Belharouak, C. S. Yoon, Y.-K. Sun, *ACS Energy Lett.* **2021**, *6*, 2726.
[13] B. A. Walker, C. O. Plaza-Rivera, S.-S. Sun, W. Lu, J. W. Connell, Y. Lin, *Electrochim. Acta.* **2020**, *362*, 137129.
[14] S. Jang, J. Kang, S. Kwak, M.-L. Seol, M. Meyyappan, I. Nam, *Micromachines* **2021**, *12*, 163.
[15] M.-L. Seol, I. Nam, E. Sadatian, N. Dutta, J.-W. Han, M. Meyyappan, *Materials* **2021**, *14*, 316.
[16] M.-L. Seol, E. Sadatian, S. Jang, C. Hill, I. Nam, J.-W. Han, M. Meyyappan, *ACS Appl. Electron. Mater.* **2020**, *2*, 3643.
[17] M.-L. Seol, I. Nam, E. L. Ribeiro, B. Segel, D. Lee, T. Palma, H. Wu, D. Mukherjee, B. Khomami, C. Hill, J.-W. Han, M. Meyyappan, *ACS Appl. Energy Mater.* **2020**, *3*, 4965.
[18] A. Maurel, A. C. Martinez, D. A. Dornbusch, W. H. Huddleston, M.-L. Seol, C. R. Henry, J. M. Jones, B. Yelamanchi, S. Bakhtar Chavari, J. E. Edmunson, S. T. Sreenivasan, P. Cortes, E. MacDonald, C. G. Sherrard, *ACS Energy Lett.* **2023**, *8*, 1042.
[19] S.-B. Hong, Y.-J. Lee, U.-H. Kim, C. Bak, Y. M. Lee, W. Cho, H. J. Hah, Y.-K. Sun, D.-W. Kim, *ACS Energy Lett.* **2022**, *7*, 1092.
[20] Y. Li, Y. Wu, Z. Wang, J. Xu, T. Ma, L. Chen, H. Li, F. Wu, *Mater. Today* **2022**, *55*, 92.
[21] W. D. Connor, S. Arisetty, K. P. Yao, K. Fu, S. G. Advani, A. K. Prasad, *J. Power Sources* **2022**, *546*, 231972.
[22] E. Mullane, T. Kennedy, H. Geaney, K. M. Ryan, *ACS Appl. Mater. Interfaces* **2014**, *6*, 18800.
[23] B. Ludwig, Z. Zheng, W. Shou, Y. Wang, H. Pan, *Sci. Rep.* **2016**, *6*, 23150.
[24] B. Ludwig, J. Liu, I. M. Chen, Y. Liu, W. Shou, Y. Wang, H. Pan, *Adv. Mater. Interfaces* **2017**, *4*, 1700570.
[25] M. Al-Shroofy, Q. Zhang, J. Xu, T. Chen, A. P. Kaur, Y.-T. Cheng, *J. Power Sources* **2017**, *352*, 187.
[26] Y. Zhang, F. Huld, S. Lu, C. Jektvik, F. Lou, Z. Yu, *Batteries* **2022**, *8*, 57.
[27] R. Tao, B. Steinhoff, X.-G. Sun, K. Sardo, B. Skelly, H. M. Meyer, C. Sawicki, G. Polizos, X. Lyu, Z. Du, J. Yang, K. Hong, J. Li, *Chem. Eng. J.* **2023**, *471*, 144300.
[28] K. Sato, Y. Tominaga, Y. Imai, T. Yoshiyama, Y. Aburatani, *Polym. Test.* **2022**, *113*, 107690.
[29] X. Wang, S. Chen, K. Zhang, L. Huang, H. Shen, Z. Chen, C. Rong, G. Wang, Z. Jiang, *Materials* **2023**, *16*, 7232.
[30] J. Wu, H. Wang, B. Feng, Y. Li, S. Wu, Q. Yin, Z. Yu, J. Huang, *Polym. Test.* **2020**, *91*, 106835.
[31] H. Kim, J. H. Lim, T. Lee, J. An, H. Kim, H. Song, H. Lee, J. W. Choi, J. H. Kang, *ACS Energy Lett.* **2023**, *8*, 3460.
[32] M. Ryu, Y.-K. Hong, S.-Y. Lee, J. H. Park, *Nat. Commun.* **2023**, *14*, 1316.
[33] X. Wei, S. Li, W. Wang, X. Zhang, W. Zhou, S. Xie, H. Liu, *Adv. Sci.* **2022**, *9*, 2200054.
[34] B. Podlesny, K. R. Hinkle, K. Hayashi, Y. Niidome, T. Shiraki, D. Janas, *Adv. Sci.* **2023**, *10*, 2207218.
[35] D. Yang, L. Li, X. Li, W. Xi, Y. Zhang, Y. Liu, X. Wei, W. Zhou, F. Wei, S. Xie, H. Liu, *Nat. Commun.* **2023**, *14*, 2491.
[36] M. H. Islam, S. Afroj, M. A. Uddin, D. V. Andreeva, K. S. Novoselov, N. Karim, *Adv. Funct. Mater.* **2022**, *32*, 2205723.
[37] C. Johnson, *Pol'y & Prac.* **2021**, *42*, 91.
[38] J. Black, A. Moreland, M. M. Ransom, E. Sanchez, *Health Matrix* **2021**, *31*, 341.
[39] N. M. Brennan, A. T. Evans, M. K. Fritz, S. A. Peak, H. E. von Holst, *Int. J. Environ. Res. Public Health* **2021**, *18*, 10900.
[40] T. Qin, H. Yang, Q. Li, X. Yu, H. Li, *Industrial Chemistry & Materials* **2024**, *2*, 191.
[41] J. E. Marshall, A. Zhenova, S. Roberts, T. Petchey, P. Zhu, C. E. J. Dancer, C. R. McElroy, E. Kendrick, V. Goodship, *Polymers* **2021**, *13*, 1354.
[42] V. F. Cardoso, D. M. Correia, C. Ribeiro, M. M. Fernandes, S. Lanceros-Méndez, *Polymers* **2018**, *10*, 161.
[43] K. Qi, Y. Wang, N. Dong, B. Liu, G. Tian, S. Qi, D. Wu, *Appl. Energy* **2022**, *320*, 119282.
[44] J. Jansta, F. P. Dousek, *Carbon* **1980**, *18*, 433.
[45] D. H. S. Tan, Y. S. Meng, J. Jang, *Joule* **2022**, *6*, 1755.
[46] M. Zhang, M. Chouchane, S. A. Shojaee, B. Winiarski, Z. Liu, L. Li, R. Pelapur, A. Shodiev, W. Yao, J.-M. Doux, S. Wang, Y. Li, C. Liu, H. Lemmens, A. A. Franco, Y. S. Meng, *Joule* **2023**, *7*, 201.
[47] T. Jiang, P. He, G. Wang, Y. Shen, C.-W. Nan, L.-Z. Fan, *Adv. Energy Mater.* **2020**, *10*, 1903376.
[48] D. Lee, A. Manthiram, *Small Methods* **2023**, *7*, 2201680.
[49] Y. Zhang, S. Lu, F. Lou, Z. Yu, *Energy Technol.* **2022**, *10*, 2200732.
[50] T. Lee, J. An, W. J. Chung, H. Kim, Y. Cho, H. Song, H. Lee, J. H. Kang, J. W. Choi, *ACS Appl. Mater. Interfaces* **2024**, *16*, 8930.
[51] M. Hendrickson, E. J. Plichta, Q. Wu, J. P. Zheng, *MRS Adv.* **2019**, *4*, 857.
[52] G. Li, R. Xue, L. Chen, *Solid State Ionics* **1996**, *90*, 221.
[53] J. Glüge, R. London, I. T. Cousins, J. DeWitt, G. Goldenman, D. Herzke, R. Lohmann, M. Miller, C. A. Ng, S. Patton, X. Trier, Z. Wang, M. Scheringer, *Environ. Sci. Technol.* **2022**, *56*, 6232.
[54] C. R. Kirman, B. R. Sonawane, J. G. Seed, N. O. Azu, W. T. Barranco, W. R. Hamilton, T. J. Stedeford, S. M. Hays, *Regulatory Toxicology and Pharmacology* **2023**, *138*, 105337.
[55] Y.-B. Wang, Q. Yang, X. Guo, S. Yang, A. Chen, G.-J. Liang, C.-Y. Zhi, *Rare Met.* **2022**, *41*, 745.
[56] D. Bresser, D. Buchholz, A. Moretti, A. Varzi, S. Passerini, *Energy Environ. Sci.* **2018**, *11*, 3096.
[57] Y. Shi, X. Zhou, G. Yu, *Acc. Chem. Res.* **2017**, *50*, 2642.
[58] R. Tao, B. Steinhoff, K. Uzun, B. La Riviere, K. Sardo, B. Skelly, R. Hill, Y.-T. Cheng, J. Li, *J. Power Sources* **2023**, *581*, 233481.
[59] D. J. Lee, J. Jang, J. P. Lee, J. Wu, Y. T. Chen, J. Holoubek, K. Yu, S. Y. Ham, Y. Jeon, T. H. Kim, *Adv. Funct. Mater.* **2023**, *33*, 2301341.
[60] T. Jiang, P. He, Y. Liang, L.-Z. Fan, *Chem. Eng. J.* **2021**, *421*, 129965.
[61] J. Kim, K. Park, M. Kim, H. Lee, J. Choi, H. B. Park, H. Kim, J. Jang, Y. H. Kim, T. Song, *Adv. Energy Mater.* **2024**, *14*, 2303455.
[62] X. Shen, H. Yu, L. Ben, W. Zhao, Q. Wang, G. Cen, R. Qiao, Y. Wu, X. Huang, *J. Energy Chem.* **2024**, *90*, 133.
[63] K. Kwon, J. Kim, S. Han, J. Lee, H. Lee, J. Kwon, J. Lee, J. Seo, P. J. Kim, T. Song, *Small Science* **2024**, *4*, 2300302.
[64] G. Xi, Z. Zhang, L. Zhong, S. Wang, M. Xiao, D. Han, S. Huang, Y. Meng, *Chem. Eng. J.* **2024**, *485*, 149983.
[65] J. Liu, B. Ludwig, Y. Liu, Z. Zheng, F. Wang, M. Tang, J. Wang, J. Wang, H. Pan, Y. Wang, *Adv. Mater. Technol.* **2017**, *2*, 1700106.
[66] L. S. Kremer, A. Hoffmann, T. Danner, S. Hein, B. Prifling, D. Westhoff, C. Dreer, A. Latz, V. Schmidt, M. Wohlfahrt-Mehrens, *Energy Technol.* **2020**, *8*, 1900167.
[67] L. S. Kremer, T. Danner, S. Hein, A. Hoffmann, B. Prifling, V. Schmidt, A. Latz, M. Wohlfahrt-Mehrens, *Batteries Supercaps* **2020**, *3*, 1172.
[68] K. Fu, X. Li, K. Sun, P. Tan, *J. Power Sources* **2024**, *591*, 233880.
[69] F. Huttner, A. Diener, T. Heckmann, J. C. Eser, T. Abali, J. K. Mayer, P. Scharfer, W. Schabel, A. Kwade, *J. Electrochem. Soc.* **2021**, *168*, 090539.
[70] Y. Kim, M. Kim, T. Lee, E. Kim, M. An, J. Park, J. Cho, Y. Son, *Electrochem. Commun.* **2023**, *147*, 107437.
[71] H. Bockholt, W. Haselrieder, A. Kwade, *ECS Trans.* **2013**, *50*, 25.
[72] G. Zhang, Y. Yang, Y. Chen, J. Huang, T. Zhang, H. Zeng, C. Wang, G. Liu, Y. Deng, *Small* **2018**, *14*, 1801189.
[73] J. He, L. Zhang, *J. Alloys Compd.* **2018**, *763*, 228.
[74] S. Huang, X. Huang, X. Li, Y. Huang, X. He, H. Zhuo, S. Chen, *New J. Chem.* **2021**, *45*, 11130.


© 2025 The Author(s). Advanced Materials published by Wiley-VCH GmbH

15214095, 2025, 12, Downloaded from https://advanced.onlinelibrary.wiley.com/doi/10.1002/adma.202416872 by Chung-Ang University, Seoul, Wiley Online Library on [23/10/2025]. See the Terms and Conditions (https://onlinelibrary.wiley.com/terms-and-conditions) on Wiley Online Library for rules of use; OA articles are governed by the applicable Creative Commons License

[75] A. Magasinski, B. Zdyrko, I. Kovalenko, B. Hertzberg, R. Burtovyy, C. F. Huebner, T. F. Fuller, I. Luzinov, G. Yushin, *ACS Appl. Mater. Interfaces* **2010**, *2*, 3004.
[76] Z. Li, W. Tang, Y. Yang, G. Lai, Z. Lin, H. Xiao, J. Qiu, X. Wei, S. Wu, Z. Lin, *Adv. Funct. Mater.* **2022**, *32*, 2206615.
[77] T. R. Martin, R. T. Pekarek, J. E. Coyle, M. C. Schulze, N. R. Neale, *J. Mater. Chem. A.* **2021**, *9*, 21929.
[78] J. Li, R. B. Lewis, J. R. Dahn, *Electrochem. Solid-State Lett.* **2007**, *10*, A17.
[79] J. Patra, P. C. Rath, C. Li, H.-M. Kao, F.-M. Wang, J. Li, J.-K. Chang, *ChemSusChem* **2018**, *11*, 3923.
[80] L. Wei, C. Chen, Z. Hou, H. Wei, *Sci. Rep.* **2016**, *6*, 19583.
[81] B. Koo, H. Kim, Y. Cho, K. T. Lee, N.-S. Choi, J. Cho, *Angew. Chem., Int. Ed.* **2012**, *51*, 8762.
[82] J. M. Foster, X. Huang, M. Jiang, S. J. Chapman, B. Protas, G. Richardson, *J. Power Sources* **2017**, *350*, 140.
[83] N.-Y. Kim, J. Moon, M.-H. Ryou, S.-H. Kim, J.-H. Kim, J.-M. Kim, J. Bang, S.-Y. Lee, *Adv. Energy Mater.* **2022**, *12*, 2102109.
[84] J.-T. Li, Z.-Y. Wu, Y.-Q. Lu, Y. Zhou, Q.-S. Huang, L. Huang, S.-G. Sun, *Adv. Energy Mater.* **2017**, *7*, 1701185.
[85] J. Entwistle, R. Ge, K. Pardikar, R. Smith, D. Cumming, *Renewable Sustainable Energy Rev.* **2022**, *166*, 112624.
[86] R. Tao, S. Tan, H. M. Meyer Iii, X.-G. Sun, B. Steinhoff, K. Sardo, A. Bishtawi, T. Gibbs, J. Li, *ACS Appl. Mater. Interfaces* **2023**, *15*, 40488.
[87] A. Zhang, J. Chai, C. Yang, J. Zhao, G. Zhao, G. Wang, *Mater. Des.* **2021**, *211*, 110157.
[88] M. Li, W. Zhang, C. Wang, H. Wang, *J. Appl. Polym. Sci.* **2012**, *123*, 1667.
[89] X. Wang, Y. Wang, X. Wang, *J. Appl. Polym. Sci.* **2023**, *140*, e54706.
[90] R. Tao, B. Steinhoff, C. H. Sawicki, J. Sharma, K. Sardo, A. Bishtawi, T. Gibbs, J. Li, *J. Power Sources* **2023**, *580*, 233379.
[91] M. Han, X. Liang, C. Han, C. Zhou, Q. Xiang, Y. Cao, J. Sun, *Adv. Funct. Mater.* **2024**, *34*, 2308325.
[92] M. P. Allen, D. J. Tildesley, *Computer Simulation of Liquids*, Oxford University Press, Oxford, England **2017**.
[93] M. E. Tuckerman, *Statistical mechanics: theory and molecular simulation*, Oxford university press, Oxford, England **2023**.
[94] J. Kang, M. Atwair, I. Nam, C.-J. Lee, *Energy* **2023**, *263*, 125801.
[95] X. Zhang, Z. Ju, Y. Zhu, K. J. Takeuchi, E. S. Takeuchi, A. C. Marschilok, G. Yu, *Adv. Energy Mater.* **2021**, *11*, 2000808.
[96] Y. Kuang, C. Chen, D. Kirsch, L. Hu, *Adv. Energy Mater.* **2019**, *9*, 1901457.
[97] Z. Wang, C. Dai, K. Chen, Y. Wang, Q. Liu, Y. Liu, B. Ma, L. Mi, W. Mao, *J. Power Sources* **2022**, *551*, 232176.
[98] C. Heubner, A. Nickol, J. Seeba, S. Reuber, N. Junker, M. Wolter, M. Schneider, A. Michaelis, *J. Power Sources* **2019**, *419*, 119.
[99] E. G. Sukenik, L. Kasaei, G. G. Amatucci, *J. Power Sources* **2023**, *579*, 233327.
[100] K.-Y. Park, J.-W. Park, W. M. Seong, K. Yoon, T.-H. Hwang, K.-H. Ko, J.-H. Han, Y. Jaedong, K. Kang, *J. Power Sources* **2020**, *468*, 228369.
[101] H. Zheng, J. Li, X. Song, G. Liu, V. S. Battaglia, *Electrochim. Acta* **2012**, *71*, 258.
[102] R. Tian, S.-H. Park, P. J. King, G. Cunningham, J. Coelho, V. Nicolosi, J. N. Coleman, *Nat. Commun.* **2019**, *10*, 1933.
[103] Z. Du, D. L. Wood, C. Daniel, S. Kalnaus, J. Li, *J. Appl. Electrochem.* **2017**, *47*, 405.
[104] C. Heubner, A. Nickol, J. Seeba, S. Reuber, N. Junker, M. Wolter, M. Schneider, A. Michaelis, *J. Power Sources* **2019**, *419*, 119.
[105] M. A. Kebede, *J. Energy Storage* **2023**, *72*, 108602.
[106] T. Konya, Y. Kobayashi, T. Nakamura, *Solid State Ionics* **2022**, *374*, 115820.
[107] A. Bhatia, Y. D. Zrelli, J.-P. Pereira-Ramos, R. Baddour-Hadjean, *J. Mater. Chem. A.* **2021**, *9*, 13496.
[108] R. Tatara, P. Karayaylali, Y. Yu, Y. Zhang, L. Giordano, F. Maglia, R. Jung, J. P. Schmidt, I. Lund, Y. Shao-Horn, *J. Electrochem. Soc.* **2019**, *166*, A5090.
[109] Y. Zhang, Y. Katayama, R. Tatara, L. Giordano, Y. Yu, D. Fraggedakis, J. G. Sun, F. Maglia, R. Jung, M. Z. Bazant, *Energy Environ. Sci.* **2020**, *13*, 183.
[110] J. Fu, D. Mu, B. Wu, J. Bi, H. Cui, H. Yang, H. Wu, F. Wu, *ACS Appl. Mater. Interfaces* **2018**, *10*, 19704.
[111] J. Lee, Y.-J. Kim, H. S. Jin, H. Noh, H. Kwack, H. Chu, F. Ye, H. Lee, H.-T. Kim, *ACS Omega* **2019**, *4*, 3220.
[112] W. Zhao, J. Zheng, L. Zou, H. Jia, B. Liu, H. Wang, M. H. Engelhard, C. Wang, W. Xu, Y. Yang, J.-G. Zhang, *Adv. Energy Mater.* **2018**, *8*, 1800297.
[113] X. Fan, G. Hu, B. Zhang, X. Ou, J. Zhang, W. Zhao, H. Jia, L. Zou, P. Li, Y. Yang, *Nano Energy* **2020**, *70*, 104450.
[114] B. P. Thapaliya, T. Wang, A. Y. Borisevich, H. M. Meyer III, X.-G. Sun, M. P. Paranthaman, C. A. Bridges, S. Dai, *Adv. Funct. Mater.* **2023**, *33*, 2302443.
[115] O. Tiurin, N. Solomatin, M. Auinat, Y. Ein-Eli, *J. Power Sources* **2020**, *448*, 227373.
[116] Q. Liu, Y. Sun, S. Wang, Q. An, L. Duan, G. Zhao, C. Wang, K. Doyle-Davis, H. Guo, X. Sun, *Mater. Today* **2023**, *64*, 21.
[117] L. Di, C. Yufang, S. Weiwei, X. Wei, Y. Shuaiyu, L. Shiqiang, Z. Lanlan, Z. Yanshuang, Y. Tianyan, X. Peitao, Z. Chunman, *Adv. Energy Mater.* **2023**, *13*, 2301765.
[118] F. Hippauf, B. Schumm, S. Doerfler, H. Althues, S. Fujiki, T. Shiratsuchi, T. Tsujimura, Y. Aihara, S. Kaskel, *Energy Storage Mater.* **2019**, *21*, 390.


© 2025 The Author(s). Advanced Materials published by Wiley-VCH GmbH

15214095, 2025, 12, Downloaded from https://advanced.onlinelibrary.wiley.com/doi/10.1002/adma.202416872 by Chung-Ang University, Seoul, Wiley Online Library on [23/10/2025]. See the Terms and Conditions (https://onlinelibrary.wiley.com/terms-and-conditions) on Wiley Online Library for rules of use; OA articles are governed by the applicable Creative Commons License